



HAL
open science

Temperature Dependence of the Collision-Induced Absorption Band of O₂ Near 1.27 μm

S. Kassi, S. Guessoum, J. Abanto, H. Tran, A. Campargue, D. Mondelain

► **To cite this version:**

S. Kassi, S. Guessoum, J. Abanto, H. Tran, A. Campargue, et al.. Temperature Dependence of the Collision-Induced Absorption Band of O₂ Near 1.27 μm . *Journal of Geophysical Research: Atmospheres*, 2021, 126 (13), pp.e2021JD034860. 10.1029/2021JD034860 . hal-03337154

HAL Id: hal-03337154

<https://hal.science/hal-03337154>

Submitted on 15 Nov 2021

HAL is a multi-disciplinary open access archive for the deposit and dissemination of scientific research documents, whether they are published or not. The documents may come from teaching and research institutions in France or abroad, or from public or private research centers.

L'archive ouverte pluridisciplinaire **HAL**, est destinée au dépôt et à la diffusion de documents scientifiques de niveau recherche, publiés ou non, émanant des établissements d'enseignement et de recherche français ou étrangers, des laboratoires publics ou privés.

27 **Abstract**

28 The 1.27 μm O_2 band is called upon to be used more and more for air-mass determination from
 29 ground-based and space-borne atmospheric spectra because of its advantages compared to the A-band at
 30 0.76 μm . For this purpose, it is important to well characterize not only the narrow absorption lines but
 31 also the strong underlying broad collision-induced absorption (CIA) structure and its temperature
 32 dependence. Spectra of O_2 and of O_2 in N_2 were recorded by cavity ring down spectroscopy (CRDS) at
 33 271 K and 332 K, with the help of a newly developed temperature regulated cell. The quality of the
 34 spectra allowed determining the small variations (at the few percent level) of the $B_{\text{O}_2-\text{O}_2}$, $B_{\text{O}_2-\text{N}_2}$ and
 35 $B_{\text{O}_2-\text{air}}$ binary coefficients with temperature. Together with the binary coefficients at 297 K reported
 36 previously, they allow characterizing the temperature dependence of the O_2 CIA at 1.27 μm in
 37 atmospheric conditions. The obtained results are compared with previous measurements by Fourier
 38 transform spectroscopy (FTS) and recent theoretical calculations. In the wings of the pure O_2 CIA, an
 39 increase with temperature is observed in agreement with calculations but contrary to the latter, a decrease
 40 is observed near the maximum of the CIA band. The temperature dependence is found in good agreement
 41 with the theoretical $B_{\text{N}_2-\text{O}_2}$ values and the experimental $B_{\text{O}_2-\text{air}}$ values derived from the FTS
 42 measurements. Binary coefficients integrated over the entire band show almost no variation with
 43 temperature for O_2-N_2 and a small increase for pure O_2 , in agreement with the theoretical predictions.

44

45 **1. Introduction**

46 Thanks to its constant volume mixing ratio of 0.2095 in the Earth's atmosphere (Goody & Yung,
 47 1989), oxygen is used as a proxy to determine sounded air- masses (Long et al., 2010; Washenfelder et
 48 al., 2006; Wunch et al., 2011). Up to very recently, the A-band of O_2 centered at 0.76 μm was preferred to
 49 retrieve air-masses from space borne instruments. The weaker $a^1\Delta_g - X^3\Sigma_g^-(0 - 0)$ band near 1.27 μm
 50 was only used by ground-based instruments as those of the Total Carbon Column Observing Network
 51 (TCCON) (Washenfelder et al., 2006) even if it presents specific advantages. First, being weaker, the 1.27
 52 μm band shows less saturated lines and reduced line-mixing effects compared to the A-band. Second, its
 53 spectral proximity with the CO_2 and CH_4 absorption bands near 1.60 μm and 1.66 μm , respectively,
 54 allows reducing uncertainties due to the aerosol scattering which spectrally varies depending on location
 55 of the sounded air-column (Bertaux et al., 2018).

56 Until recently, the strong mesosphere/stratosphere airglow produced by O_3 photo-dissociation
 57 limited the use of the 1.27 μm band to ground-based remote sensing. But, Bertaux et al. (2018) and Sun et
 58 al. (2018) managed to accurately model this effect rendering this band suitable for space-borne
 59 observations. Hence, as a comparative test, both the A- and 1.27 μm bands will be covered by the

60 *MicroCarb* satellite dedicated to the accurate determination of CO₂ in the troposphere, that should be
 61 launched in 2021 (CNES, 2018). In order to achieve a targeted accuracy on the column-averaged CO₂
 62 mole fraction better than 1 ppm (i.e. 0.3% in relative), an accurate derivation of the dry air column is
 63 mandatory. To achieve this goal, the rovibronic lines of the 1.27 μm band must be accurately
 64 characterized together with the underlying CIA. This is all the more crucial as about half of the total O₂
 65 absorption of the 1.27 μm band is due to the CIA for 1 amagat of air.

66 Note that the heat balance of the Earth's atmosphere is affected by the O₂ CIA bands which overall
 67 contribute to absorption of about 1 Wm⁻² (Zender, 1999). About 22% of this contribution (integrated
 68 between 5000 and 30000 cm⁻¹) is due to the 1.27 μm band.

69 O₂ bands could also be used as a marker of the oxygenic photosynthesis (Misra et al., 2014,
 70 Schwieterman et al., 2018) and bring constraints on the atmospheric pressures of the Earth's like
 71 exoplanets. Hence, Misra et al., (2014) showed that atmospheric pressures could be retrieved from pure
 72 bound and quasi-bound O₂ complexes in the near infrared for a certain range of pressures and O₂ volume
 73 mixing ratios. They also calculated that the CIA of the 1.27 μm band should be detectable in some cases
 74 during transit transmission spectroscopy by the future *James Webb Space Telescope* (Gardner et al.,
 75 2006).

76 In the $a^1\Delta_g - X^3\Sigma_g^-(0-0)$ band centered near 1.27 μm, the electric dipole rovibronic transitions
 77 are forbidden by both spin ($S = 1 \rightarrow 0$) and spatial ($g \rightarrow g$) selection rules. Monomer absorption is thus
 78 due to the (weak) spin-orbit-allowed magnetic dipole transitions and even weaker electric quadrupole
 79 transitions and (1-1) hot band transitions (Gordon et al., 2010; Leshchishina et al., 2010). These
 80 monomer lines are superimposed to the CIA continuum coming from the transient electric dipole induced
 81 by collisions of O₂-O₂ and O₂-N₂ molecules (Gordon et al., 2017; Solomon et al., 1998). Note that in our
 82 atmosphere, the absorption coefficient integrated over an absorption line is proportional to the O₂ density,
 83 ρ_{O_2} , while the CIA involves a self-component proportional to ρ_{O_2} squared and a foreign component
 84 proportional to $\rho_{O_2}\rho_{N_2}$.

85 The CIA of the 1.27 μm band has been studied experimentally with grating or Fourier transform
 86 (FT) spectrometers at room temperature and below since more than 60 years (Badger et al., 1965;
 87 Blickensderfer et al., 1969; Chagas et al., 2002; Cho 1963; Dianov-Klokov, 1964; Ketelaar, 1955; Maté et
 88 al., 1999; McKellar et al., 1972; Smith et al., 1999; Tabisz et al., 1969), but only a few studies (Chagas et
 89 al., 2002; Maté et al., 1999; Newnham and Ballard, 1998; Smith and Newnham, 2000) reported cross-
 90 sections with reasonable signal-to-noise ratio because of the quite weak CIA absorption. For this reason,

91 all these previous studies used long absorption path lengths and sample pressures at atmospheric
92 pressures or above.

93 Recently, cavity enhanced absorption techniques like cavity-ring-down spectroscopy (CRDS) have
94 been applied to the O₂ CIA measurements (Karman et al., 2018; Mondelain et al., 2019) and more
95 generally to the continua measurements (see for example Campargue et al., 2016 and references herein;
96 Lechevallier et al., 2018; Mondelain et al., 2017 and references herein; Richard et al., 2017). These
97 techniques were found particularly suitable as they provide both a high sensitivity and a high baseline
98 stability of the spectra.

99 The present work follows our CRDS study of the 1.27 μm CIA at room temperature (Mondelain et
100 al., 2019) in support of the *MicroCarb* satellite mission. Here, we focus on the temperature dependence of
101 the CIA *i.e.* of the $B_{O_2-O_2}$, $B_{O_2-N_2}$, and B_{O_2-air} binary absorption coefficients. For this purpose, a
102 temperature regulated CRDS cell has been developed and spectra of pure O₂ and of O₂ in N₂ were
103 recorded at 271 K and 332 K between 7550 and 8360 cm⁻¹. Overall, the set of measurements at three
104 temperatures allows for the determination of the temperature dependence of the O₂ CIA at 1.27 μm in the
105 range of the atmospheric temperatures. This study, together with the recent works devoted to the
106 absorption lines (Konefał et al., 2020; Tran et al., 2020), will help to meet the spectroscopic accuracy
107 requirements of the *MicroCarb* satellite mission. In the next part (Part 2), the experimental set-up and the
108 adopted experimental strategy are presented. The spectra analysis and retrieval of the binary absorption
109 coefficients are presented in Part 3. The comparison of the obtained temperature dependence with those
110 from FTS measurements of Maté et al. (1999) and calculations of Karman et al. (2018) is discussed in
111 Part 4 and perspectives are drawn up in Part 5.

112 2. Experimental set-up

113 The high sensitivity and baseline stability of the continuous wave CRDS technique (Berden et al.,
114 2000; Maity et al., 2021; Romanini et al., 1997) have been largely demonstrated during the last years
115 (Campargue et al., 2016 and references herein; Kassi et al., 2012). Reader is referred to (Kassi et al.,
116 2012; Mondelain et al., 2019) for the presentation of our CRDS setup. For this project, we developed a
117 temperature regulated high finesse cavity (HFC) (**Figure 1**) using the circulation of a coolant as adopted
118 in Ghysels et al. (2017).

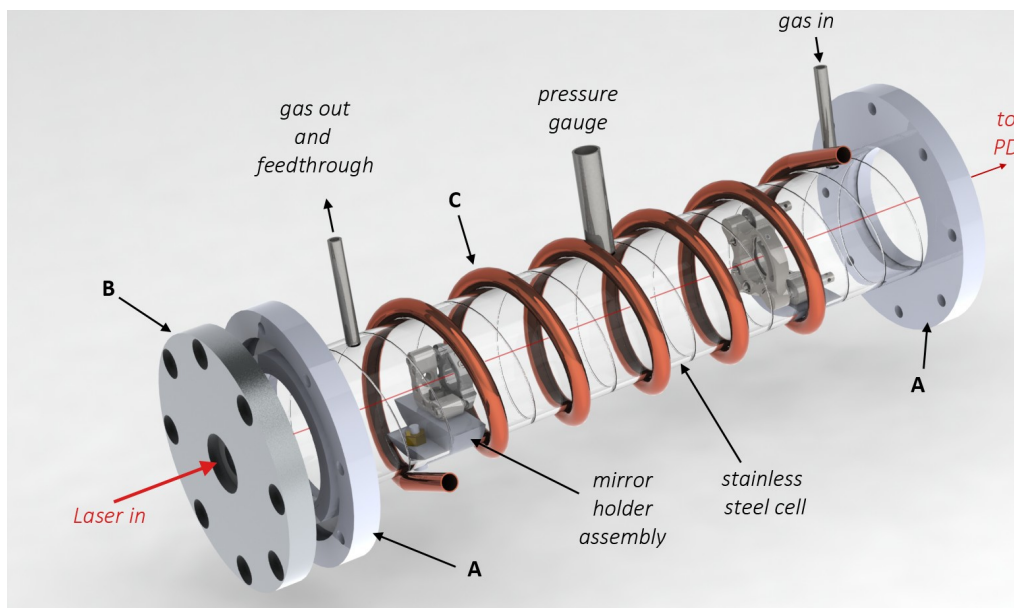
119 2.1. The temperature regulated high finesse cavity

120 Two high reflectivity mirrors from Layertec ($R > 99.99\%$ over the 1170 nm-1370 nm range),
121 separated by 500 mm, were placed inside a stainless steel tube (700 mm long, 63 mm external diameter)
122 fitted with two receptacle flanges at both ends. Outer flanges, housing anti-reflective and wedged

123 windows, are bolted to the receptacle with a Viton o-ring ensuring the tightness. This aspect is inherited
 124 from previous liquid nitrogen cooled setup (Kassi et al., 2008) and high pressure CRDS setup (Kassi et
 125 al., 2015). The gas is therefore free to circulate around the mirrors.

126 The tube was thermalized thanks to two counter-propagating copper coils through which a cooling
 127 fluid flows. A non-flammable, low vapor pressure silicone oil has been chosen as the heat transfer fluid.
 128 Its temperature was regulated using a deported refrigerated/heating circulator (model Corio 1000F from
 129 Julabo). Thanks to the counter-propagating arrangement, temperature gradients were averaged out,
 130 ensuring a uniform temperature of the cell envelope. Thanks to this highly symmetric conception, thermo-
 131 mechanical gradients were essentially self-compensated allowing for preservation of the optical
 132 alignment, which was done at room temperature, after several temperature cycles from -20 to +60°C.

133 To further homogenize the gas temperature and limit convection, a copper tube (1 mm thick, 30
 134 mm outer diameter), resting on two isolating shims, was installed between the two high reflectivity
 135 mirrors to closely surround the probed gas. Four 3-wires 1000 Ω platinum temperature sensors ($\frac{1}{3}$ DIN
 136 class B from -50°C to 150°C) were installed at the surface of the copper tube to determine the sample
 137 temperature. Maximum gradients of 0.3 K and 0.5 K along the HFC axis were measured at 270 K and 332
 138 K, respectively, which reads as 0.2% relative. A satisfactory long term stability of the temperature was
 139 observed. Over several weeks, internal copper tube temperature fluctuated between 331.50 K and 331.65
 140 K and between 270.1 K and 270.8 K for 333.15 K and 268.15 K coolant set points, respectively.



141
 142 **Figure 1.** Scheme of the temperature regulated cavity ring down cell developed for the present
 143 study. Here *A*, *B* and *C* correspond to the receptacle and outer flanges and to the copper coil, respectively.
 144 The CRD setup is enclosed in a thermalized chamber. The gas is free to circulate all around the mirrors.

145 The temperature is adjusted by circulating temperature regulated fluid in two contra-propagating copper
 146 coils. For clarity, the second coil and the internal copper tube (see text) are not shown and the length of
 147 the cell is not to scale. One of the mirror is actually hold on a PZT actuator (not shown) allowing for
 148 cavity length dithering. Electrical wires of the Pt1000 probes and PZT are passing through the gas tubing.

149 2.2. *Spectra acquisition*

150 Eleven distributed feed-back (DFB) fibered laser diodes and one external cavity laser diode
 151 (ECDL) were used as CRDS light sources. The 7550-7920 cm^{-1} range was covered with the DFB diode
 152 lasers; each of them allowing for a 30 cm^{-1} spectral coverage. The ECDL was used to cover the 7920-
 153 8360 cm^{-1} range. The emitted light wavenumber was measured during each scan by sending a part of the
 154 beam to a wavelength meter (Bristol 621-A IR or HighFinesse WSU7-IR). Following a cw-CRDS scheme
 155 (Morville et al. 2004), the cavity length was dithered with a PZT element supporting the output mirror.
 156 With the DFB laser diodes, the spectra were recorded with a spectral step equal to $3 \times 10^{-3} \text{ cm}^{-1}$ or 5×10^{-3}
 157 cm^{-1} depending on the gas pressure/density. At each spectral step of a scan, several ring down events were
 158 acquired, fitted with an exponential fit and averaged, providing an averaged RD time, τ . With the ECDL,
 159 in order to increase the scan speed, no effort was done to discipline it. Only its grating was scanned,
 160 leading to spectral steps of typically of 0.1 cm^{-1} , induced by the laser cavity modes. The RD events and
 161 corresponding wavenumbers were recorded *on the fly*, when scanning the ECDL over its entire emission
 162 range, taking about 2 hours per spectrum.

163 For each laser diode and for the ECDL, the procedure consisted in recording in static regime a
 164 series of spectra corresponding to two consecutive spectra with the cell filled by pure O_2 (99.9999%
 165 purity) or a mixture of O_2+N_2 (with an O_2 relative concentration of $20.965 \pm 0.044\%$ (2σ);
 166 $\text{O}_2+\text{N}_2 > 99.9999\%$ provided by Air Liquide), framed by two argon spectra (99.9999% purity) for the base
 167 line determination (**Figure 2**). The cell was entirely pumped between the gas changes. As this procedure
 168 was time consuming (typically 5 hours for the four spectra recorded for each diode), contrary to our
 169 previous CIA study at room temperature (Mondelain et al., 2019), only one pressure was recorded for a
 170 given laser diode. In addition to the superposition of the two argon spectra recorded for one diode, the
 171 baseline stability was checked with the overlap spectral range between two consecutive laser diodes as
 172 illustrated in **Figure 2**. For pure O_2 , the cell was filled at different pressures from 300 Torr to 750 Torr
 173 depending of the CIA amplitude, while for the O_2+N_2 mixture, a pressure of 700 Torr was adopted. These
 174 gas pressures were measured with a heated absolute capacitance manometer (model AA02A from MKS
 175 instruments; 1000 mbar full scale; accuracy: 0.12% of the reading).

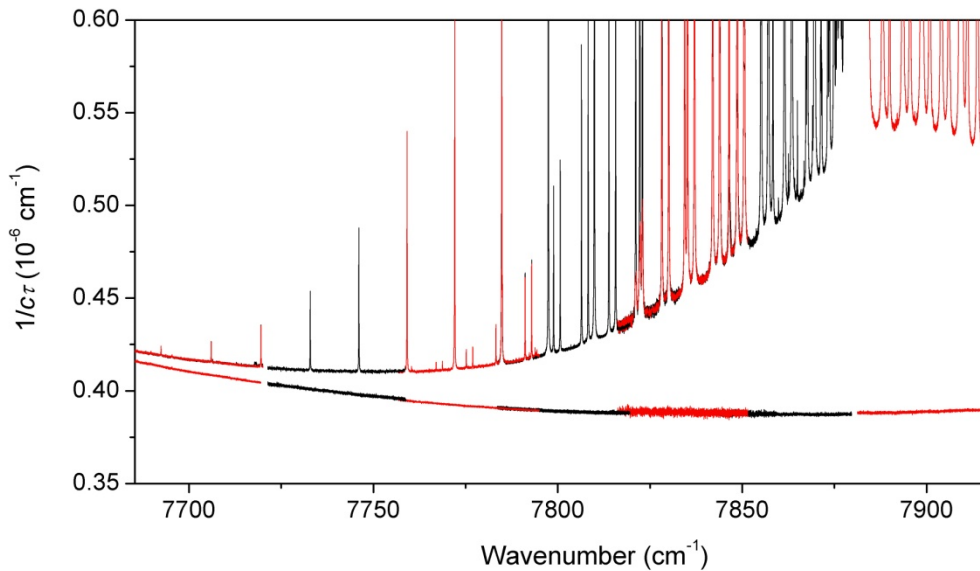
176 The extinction coefficient, $\alpha(\nu)$, corresponds to the difference between the loss rates for the cell
 177 filled with pure O₂ or O₂+N₂ gas mixture, $n/c\tau$ and with a non-absorbing gas (i.e. argon in our case),
 178 $n_{Ar}/c\tau_0$,

$$179 \quad \alpha(\nu) = \frac{n}{c\tau(\nu)} - \frac{n_{Ar}}{c\tau_0(\nu)} \quad (1)$$

180 where c is the speed of light and n and n_{Ar} , are the refractive indexes of the absorbing gas and
 181 argon, respectively. $1/c\tau_0$ is related to the reflectivity of the mirrors, R , and the cavity length, L_{cav} :

$$182 \quad \frac{n_{Ar}}{c\tau_0(\nu)} = \frac{1 - R(\nu)}{L_{cav}} \quad (2)$$

183 The RD time, τ_0 , varied from 90 μ s at 7870 cm^{-1} to 67 μ s at 7550 cm^{-1} for the cell filled with argon.
 184 The measured extinction coefficient is the sum of contributions from the O₂ monomer lines, the O₂ CIA
 185 and Rayleigh scattering.



186
 187 **Figure 2.** CRDS spectra recorded with different DFB laser diodes (red/black solid lines) for the
 188 O₂+N₂ mixture (upper spectra) and argon (lower spectra) at a total pressure of 700 Torr and a temperature
 189 of 271.2 K. The argon baseline is mostly due to the mirror reflectivity curve and includes a small
 190 Rayleigh scattering contribution. Note the good superposition of the baselines recorded at different days.

191 Spectra were recorded by scanning the DFB laser diode temperature leading to minimum detectable
 192 absorption coefficient (evaluated as the *rms* of the baseline fluctuation), α_{min} , between $2 \times 10^{-10} \text{ cm}^{-1}$ and
 193 $5 \times 10^{-10} \text{ cm}^{-1}$, for the cell filled with argon, depending on the DFB laser diode. The excess of noise

194 observed on **Figure 2** between 7820 cm^{-1} and 7860 cm^{-1} was due to the low emitted power of one of the
 195 DFB laser diode.

196 3. Spectra analysis

197 3.1. Retrieval of the binary coefficients

198 First, the spectrum baseline due to the mirror losses has to be subtracted to the oxygen (or N_2+O_2
 199 mixture) spectra. After removal of some water vapor absorption lines (present as an impurity at the ppm
 200 level in argon), the argon spectra were fitted with a second order polynomial function for each DFB laser
 201 diode and a fourth order polynomial for the ECDL. After this baseline correction, the small contribution
 202 due to Rayleigh scattering was considered and removed. The Rayleigh scattering cross-sections of Ar and
 203 O_2 being very close (Thalman et al., 2014; Thalman et al., 2017), its impact on the extinction coefficient
 204 is very small ($\sim 3 \times 10^{-11} \text{ cm}^{-1}$ at 700 Torr and 331K) which leads to a negligible correction on the
 205 $B_{\text{O}_2-\text{O}_2}$ measurements. In case of air, the difference with Ar is more important and leads to a linear
 206 variation increasing from $3.9 \times 10^{-10} \text{ cm}^{-1}$ at 7690 cm^{-1} to $5.0 \times 10^{-10} \text{ cm}^{-1}$ at 8150 cm^{-1} for a pressure of 700
 207 Torr and a temperature of 270 K (Thalman et al., 2014; Thalman et al., 2017). This weak effect was taken
 208 into account in the determination of the $B_{\text{O}_2-\text{N}_2}$, binary coefficients.

209 The remaining absorption coefficient is expressed by:

$$210 \alpha_{\text{O}_2}(v) = B_{\text{O}_2-\text{O}_2}(v)\rho_{\text{O}_2}^2 + M_{\text{O}_2}(v)\rho_{\text{O}_2} \quad (3)$$

211 for pure O_2 , and by:

$$212 \alpha_{\text{O}_2+\text{N}_2}(v) = B_{\text{O}_2-\text{O}_2}(v)\rho_{\text{O}_2}^2 + M_{\text{O}_2}(v)\rho_{\text{O}_2} + B_{\text{O}_2-\text{N}_2}(v)\rho_{\text{O}_2}\rho_{\text{N}_2} \quad (4)$$

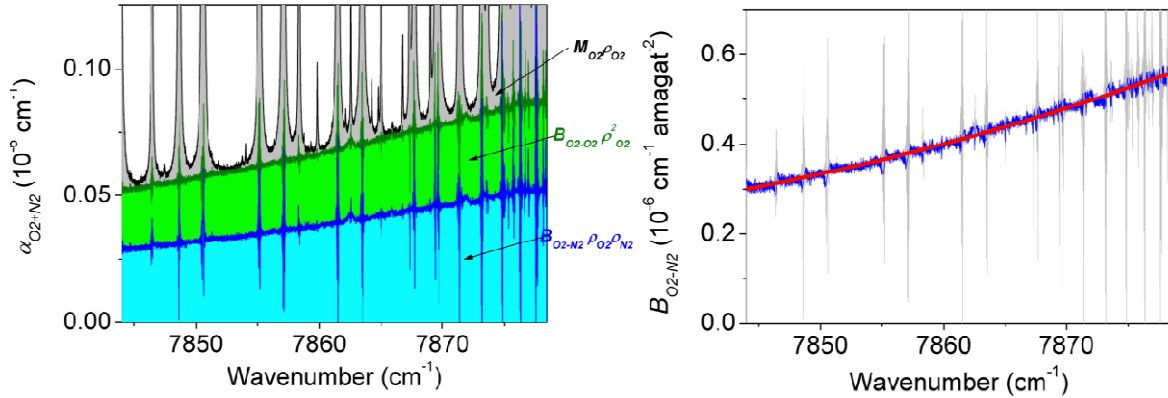
213 for the N_2+O_2 mixture.

214 Where ρ are densities in amagat, $B_{\text{O}_2-\text{O}_2}$ and $B_{\text{O}_2-\text{N}_2}$ are the binary collision absorption coefficients
 215 in $\text{cm}^{-1} \text{ amagat}^2$. $M_{\text{O}_2}(v)\rho_{\text{O}_2}$ is the local monomer contribution due to the $1.27 \mu\text{m}$ band of O_2 that was
 216 generated using the most recent spectroscopic data [see (Tran et al., 2021) and references therein]. A
 217 speed dependent Nelkin-Ghatak profile was used for these intense lines and a Voigt profile for the others,
 218 with a cutoff value of $\pm 5 \text{ cm}^{-1}$ from the line center. It was also necessary to include the line mixing effect
 219 for the Q - and R -branches region near 7890 cm^{-1} (Tran et al., 2020). This calculated line contribution was
 220 subtracted from the spectrum as illustrated on **Figure 3**. Note that the obtained residuals included in
 221 **Figure 3** show some large values which have an experimental origin: the very strong absorption due to
 222 the O_2 lines leads to very short ring down times and a low level of photons exiting the HFC and thus a
 223 high noise level.

224 The ideal gas law was applied to calculate the densities as the deviation from this law, due to the
 225 second virial coefficient, does not exceed 0.06% in the worst case. Due to desorption from the gas cell,
 226 water vapor absorption lines were observed in some spectra at 332 K and were removed using a Voigt fit

227 of their profile (the corresponding relative concentration of water vapor was typically of few ppm).
 228 $B_{O_2-O_2}$ coefficients derived from the oxygen spectra (Eq. 3) were used to subtract the O_2-O_2 contribution
 229 from the spectra of the N_2+O_2 mixture and derive the $B_{O_2-N_2}$ coefficients (Eq. 4). As illustrated in **Figure**
 230 **3** for the N_2+O_2 mixture, the O_2-O_2 and N_2-O_2 contributions are on the same order of magnitude near the
 231 band maximum.

232 The following procedure, illustrated on the right panel of **Figure 3**, was used to provide smooth
 233 curves for the binary coefficients *versus* the wavenumber. After calculation of the uncertainties of the
 234 binary coefficients, as described below, the data points with the strongest uncertainties (i.e. at the location
 235 of the absorption lines), were removed. The entire “cleaned” CIA band was then divided into a few
 236 spectral intervals (typically $\sim 150\text{ cm}^{-1}$ wide) over which a polynomial fit was performed. The
 237 concatenated fit results were then interpolated with a 1 cm^{-1} spectral step.



238
 239 **Figure 3.** Retrieval of the binary coefficients

240 *Left panel:* Different contributions to the absorption coefficient, $\alpha_{O_2+N_2}(\nu)$, measured with the
 241 DFB laser diode centered at 1270 nm for a mixture of N_2+O_2 at a total pressure of 700 Torr and a
 242 temperature of 331.6 K,

243 *Right panel:* Retrieved binary absorption coefficient, $B_{O_2-N_2}$. Refer to the text and Eq. (4) for the
 244 different notations. Data point before (grey solid line) and after (blue solid line) data cleaning using the
 245 calculated uncertainties are shown together with the result of the fit to the cleaned data corresponding to
 246 the recommended $B_{O_2-N_2}$ values (red solid line).

247
 248 **Figure 4** presents an overview of the obtained values of the $B_{O_2-O_2}$ and $B_{O_2-N_2}$ coefficients at
 249 270.5 K and 331.6 K, as provided in the *Supplementary material*.

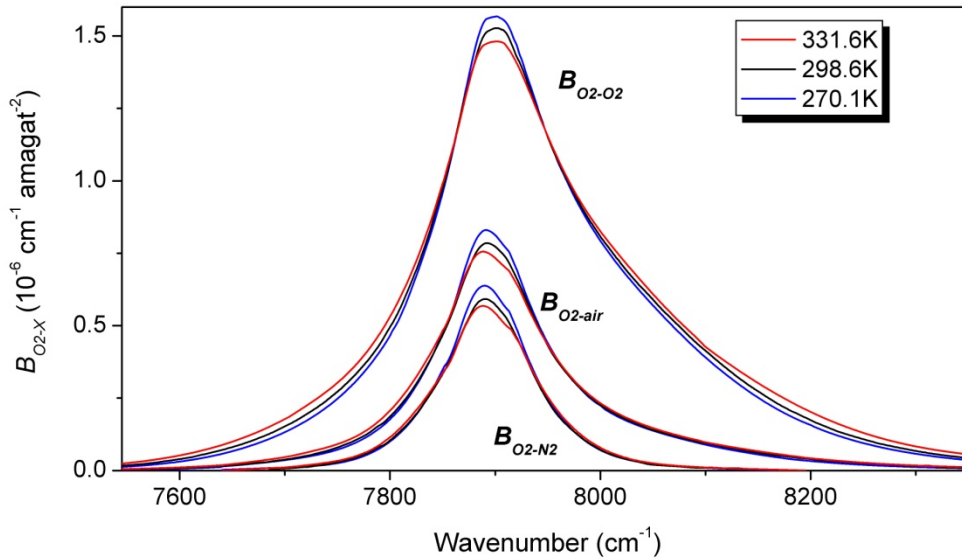
250 For atmospheric applications, it is convenient to introduce the B_{O_2-air} coefficient defined by:

251
$$\alpha_{CIA}(\nu) = B_{O_2-air}(\nu) \rho_{O_2} \rho_{air} \quad (5)$$

252 where ρ_{air} is the dry air density. The relative concentrations of nitrogen, oxygen and argon in dry air
 253 are 78.08, 20.95 and 0.93 %, respectively. The O_2 CIA induced by argon is expected to be very close to
 254 that due to nitrogen (Karman et al., 2018). Thus, the B_{O_2-air} values computed as:

$$255 \quad B_{O_2-air} = 0.2095B_{O_2-O_2} + (1 - 0.2095)B_{O_2-N_2} \quad (6)$$

256 are provided as *Supplementary Material* at both temperatures.



257 **Figure 4.** Recommended binary coefficients obtained in this work at 270.1 K and 331.6 K and in
 258 (Mondelain et al., 2019) at room temperature.
 259

260 We have gathered in **Figure 4**, the binary coefficients obtained in this work at 270.1 K and 331.6 K
 261 with the results at room temperature reported in (Mondelain et al., 2019). Let us note the consistency of
 262 the results of the two studies performed with different CRDS set ups (for instance the length of the CRDS
 263 cell used at room temperature was 140 cm to be compared to 50 cm in the present recordings). Although
 264 the changes of the CIA shape with temperature are relatively weak, the room temperature curves are
 265 systematically intermediate between the 270.1 K and 331.6 K curves. The main variations are observed at
 266 the center of the band with a decrease of the binary coefficients with the temperature (maximum variation
 267 of 5.7% between 270.1 K and 331.6 K). An opposite behavior occurs in the wings of the pure O_2 CIA.

268 Using the three temperature values at disposal, the $B_{O_2-X}(v_i)$ values can be plotted *versus* T ($X=$
 269 O_2 , N_2 and air). At each spectral step, v_i , a mostly linear dependence with the temperature is observed
 270 over the 270-331 K interval (**Figure 5** left panel). The corresponding slope $(dB/dT)_{O_2-X}(v_i)$ was
 271 obtained from a linear fit of the $B_{O_2-X}(v_i)$ values at the three temperatures. The frequency dependence of
 272 the dB/dT is presented on the right panel of **Figure 5**. As expected, the strongest (negative) temperature

273 coefficients are located near the band maximum at 7900 cm^{-1} for both $\text{O}_2\text{-O}_2$ and $\text{O}_2\text{-N}_2$. In the wings, both
 274 $\text{O}_2\text{-O}_2$ and $\text{O}_2\text{-N}_2$ coefficients increase with temperature but the effect is more pronounced for $\text{O}_2\text{-O}_2$. A
 275 small asymmetry of the dB/dT profiles can be noted for the different curves.

276 In the Supplementary Material, we provide for each CIA ($\text{O}_2\text{-O}_2$, $\text{O}_2\text{-N}_2$, $\text{O}_2\text{-air}$), the binary
 277 coefficients at 271, 297 and 332 K and the corresponding temperature dependence coefficients and
 278 estimated uncertainties. A sample of the Supplementary Material is presented in **Table 1**.

279

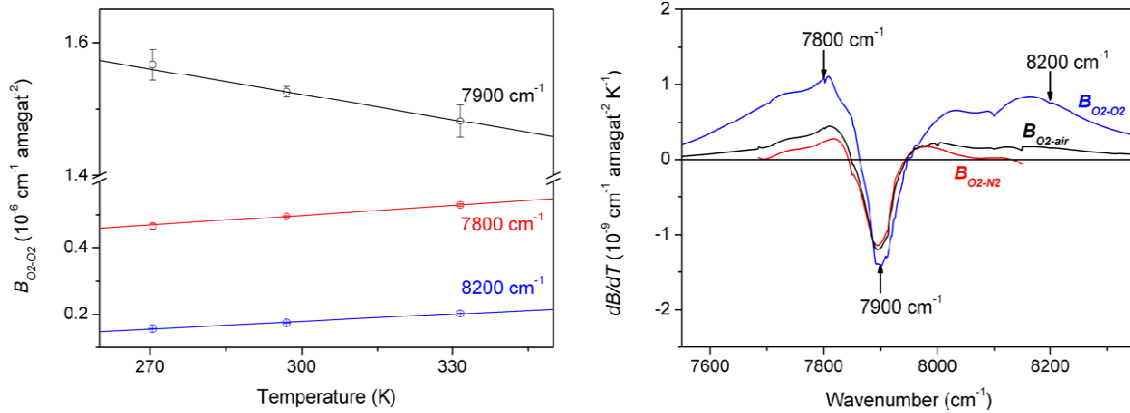
280 **Table 1.** Sample of the Supplementary material provided for $B_{\text{O}_2\text{-air}}$.

281 Experimental CRDS $B_{\text{O}_2\text{-air}}$ binary coefficients obtained from this work (at 271 K and 332 K) and from
 282 Mondelain et al. (2019) at 297 K. Values between parenthesis are estimated error bars given in the unit of
 283 the last quoted digit.

284

<i>Spectral step</i> (cm^{-1})	$B_{\text{O}_2\text{-air}}$			$dB_{\text{O}_2\text{-air}}/dT$ ($10^{-6}\text{ cm}^{-1}\text{ amagat}^2\text{ K}^{-1}$)
	271K	297K	332K	
7920	0.6980(138)	0.6667(50)	0.6464(109)	$-6.59(41)\times 10^{-4}$
7921	0.6889(134)	0.6588(50)	0.6398(109)	$-6.18(40)\times 10^{-4}$
7922	0.6784(131)	0.6509(49)	0.6332(108)	$-5.56(35)\times 10^{-4}$
7923	0.6680(128)	0.6429(49)	0.6266(107)	$-4.94(30)\times 10^{-4}$
7924	0.6584(127)	0.6349(49)	0.6188(107)	$-4.46(29)\times 10^{-4}$
7925	0.6488(126)	0.6271(48)	0.6108(106)	$-4.00(26)\times 10^{-4}$
7926	0.6390(126)	0.6190(48)	0.6027(106)	$-3.70(22)\times 10^{-4}$
7927	0.6290(125)	0.6109(48)	0.5946(105)	$-3.41(17)\times 10^{-4}$
7928	0.6195(124)	0.6027(47)	0.5866(105)	$-3.18(15)\times 10^{-4}$
7929	0.6101(124)	0.5943(47)	0.6464(109)	$-2.98(13)\times 10^{-4}$
7930	0.6008(123)	0.5859(47)	0.5711(104)	$-2.79(12)\times 10^{-4}$

285



286

Figure 5. Temperature dependence of the binary coefficients.

287

288 *Left panel:* Example of the variation of the experimental binary coefficient, $B_{O_2-O_2}$, with
 289 temperature at 7800, 7900 and 8200 cm^{-1} . Experimental values at 297 K were taken from (Mondelain et
 290 al., 2019).

291 *Right panel:* Fitted temperature coefficients, dB/dT , of $B_{O_2-X}(v_i)$ with $X=O_2, N_2$ and air.

292 **3.2. Error budget**

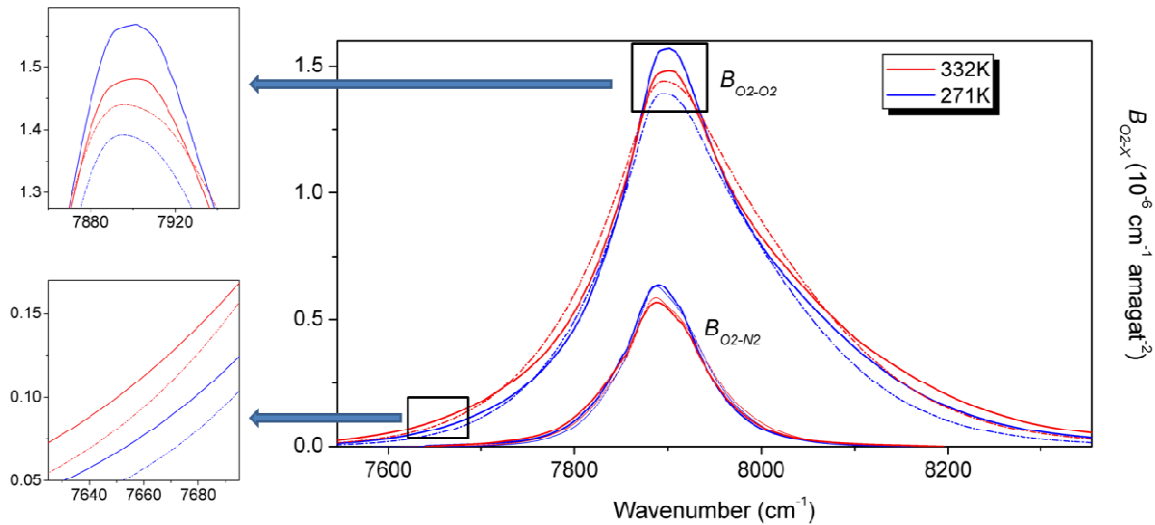
293 Uncertainties on the retrieved binary absorption coefficients have been calculated with the
 294 propagation of error approach using Eqs. (3) and (4) and assuming uncorrelated variables.

295 The base line stability was systematically checked for each series of spectra by comparing the
 296 argon spectra recorded before and after the absorbing gas spectra (see **Figure 2**). Stability of $5 \times 10^{-10} \text{ cm}^{-1}$
 297 or below was achieved except for two series where a degraded stability of $\sim 1 \times 10^{-9} \text{ cm}^{-1}$ was observed.
 298 These values were adopted as the uncertainties on α_{O_2} and $\alpha_{O_2+N_2}$. Uncertainties on the densities,
 299 calculated from the pressure gauge and temperature sensor accuracies together with gas stated purity and
 300 concentrations, are typically around 0.15%. To estimate the uncertainty coming from the subtracted
 301 monomer contribution we applied the method proposed in (Ptashnik et al., 2007). As explained above, we
 302 removed the data points with the largest uncertainties, corresponding to the location of the absorption
 303 lines so that this latter contribution becomes marginal for the “cleaned” data points.

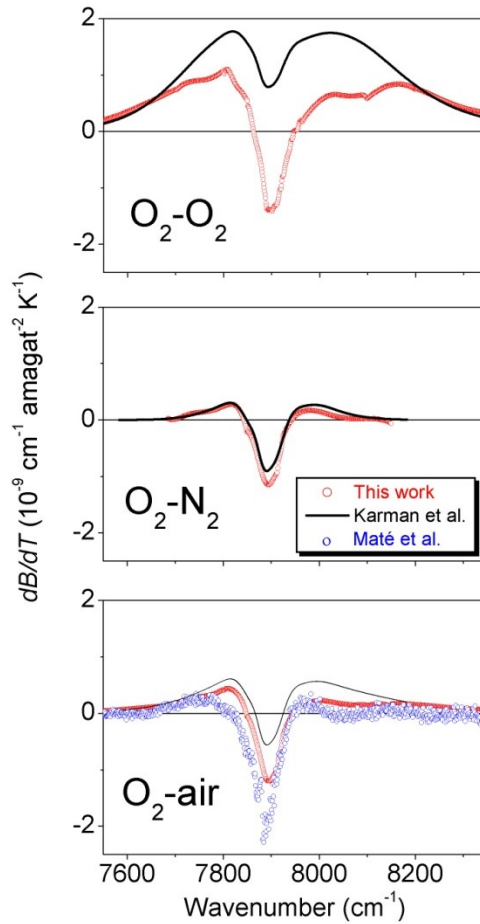
304 The resulting absolute uncertainties (1σ) of the different binary coefficients are included in the
 305 *Supplementary Material*. Over a large part of the absorption band, uncertainties better than 3% and 5%
 306 have been achieved for O_2-O_2 CIA and O_2-N_2 CIA, respectively. Note that, for the uncertainties on dB/dT ,
 307 given by the linear fit, the uncertainties on the binary coefficients were not included leading to an
 308 underestimation on that reported uncertainties.

309 **4. Comparison to literature**

310 Let us discuss our CRDS results in comparison to the previous measurements of Maté et al. (1999),
 311 and to the theoretical calculations of Karman et al. (2018). Maté et al. (1999) used an FT spectrometer
 312 with high densities gas samples (between 1 and 10 amagat) at three temperatures: 253, 273, and 296 K
 313 with an absorption path length of 84.05 m. The theoretical approach of Karman et al. (2018) used
 314 analytical models and numerical quantum scattering calculations. The spin-orbit and exchange
 315 mechanisms have been identified to break the spin symmetry in the studied collision complexes (Karman
 316 et al., 2017; Karman et al., 2018). Through quadrupole induction, these two mechanisms lead to transition
 317 dipole moments responsible of the CIA of the considered $a^1\Delta_g - X^3\Sigma_g^-(0-0)$ band of O_2 . The FTS
 318 and calculated O_2 CIA cross-sections of the considered $1.27\ \mu\text{m}$ band of O_2 are provided in the updated
 319 version of the CIA section of the HITRAN database (Karman et al., 2019).



320
 321
 322 **Figure 6.** Comparison of the binary coefficients obtained experimentally at 270.1 K and 331.6 K in
 323 this work with the theoretical values derived from Karman et al. (2018) at 271K and 332 K for $B_{O_2-O_2}$
 324 and 275 K and 323 K for $B_{O_2-N_2}$. Note that room temperature data are not shown for clarity reasons.



325
 326 **Figure 7.** Comparison of the temperature dependence of the $B_{O_2-O_2}(v_i)$ (upper panel), $B_{O_2-N_2}(v_i)$
 327 (middle panel) and $B_{O_2-air}(v_i)$ (lower panel) binary coefficients derived from CRDS measurements
 328 (This work), FTS measurements (Maté et al., 1999) and theoretical calculations (Karman et al., 2018).
 329

330 **Figure 6** presents an overview comparison of our binary coefficients with the calculated values
 331 from Karman et al., (2018) at 271 K and 332 K. At the scale of the overview, a general agreement in
 332 observed. For a more detailed comparison, it is worth comparing the dB/dT derivatives as displayed on
 333 **Figure 7**. In the same way as done for the CRDS values, dB/dT values were derived, for each
 334 wavenumber value, from a linear fit of the B values of Maté et al. (1999) (at 253, 273 and 296 K) and
 335 Karman et al. (2018) (at 271, 296 and 332 K for $B_{O_2-O_2}$ and 275, 298 and 323 K for $B_{O_2-N_2}$ and
 336 B_{O_2-air}).

337 Even if slightly more negative temperature coefficients are obtained around the band center in the
 338 case of Maté et al. (1999), the FTS and CRDS results for air are close (Maté et al. (1999) did not report
 339 binary coefficients for O_2-O_2 and O_2-N_2 at temperatures other than 296 K). Considering the different

340 experimental techniques, range of pressure values used in the two studies and the limited temperature
341 dependence of the CIA, the achieved agreement provides a mutual validation and can be considered as
342 very satisfactory.

343 Compared to Karman et al. (2018) a very good agreement is observed for the O₂-N₂ CIAs. It is
344 interesting to mention that only the spin-orbit mechanism is present for the O₂-N₂ collision complexes
345 leading to the conclusion that this mechanism is well theoretically characterized in Karman et al. (2018)
346 in the case of O₂-N₂.

347 The situation is less satisfactory for the O₂-O₂ temperature dependence. Far from the center, the
348 temperature evolution is also well predicted by calculations, but, closer to the center, large differences are
349 visible. In particular, according to the calculations, the O₂-O₂ CIA absorption is predicted to increase for
350 all the wavenumber values while our measurements reveal a significant negative temperature dependence
351 between 7860 cm⁻¹ and 7950 cm⁻¹. In the case of pure O₂ CIA, the exchange mechanism contributes to the
352 CIA in addition to the spin-orbit mechanism. As shown in Fig. 4 of Karman et al. (2018), the spin-orbit
353 mechanism leads to a relatively narrow band shape dominating in the center of the O₂-O₂ CIA band while
354 the exchange mechanism leads to a broad contribution dominating in the wings, with an equivalent
355 contribution of the two mechanisms around 20 cm⁻¹ from the center. Our observations indicate that the
356 positive temperature dependence of the exchange mechanism is overestimated by the calculations and/or
357 that the negative temperature dependence of the spin-orbit mechanism (around the center) is
358 underestimated for O₂-O₂ CIA.

359 **Table 2** lists the CRDS, FTS and calculated integrated band intensities, S_{O_2-X} ($X= O_2, N_2$ or air),
360 corresponding to the integration of the fitted binary coefficients B_{O_2-X} over the entire spectral range. The
361 obtained values are compared in **Figure 8**. Note that, in order to reproduce quantitatively the experimental
362 results of Maté et al. (1999), scaling factors have been applied at room temperature to the theoretical line
363 shapes corresponding to the exchange and spin-orbit mechanisms (Karman et al., 2018). As already noted
364 in Mondelain et al. (2019), a very satisfactory overall agreement is found when comparing our data to the
365 FTS values. Even if some small shape differences are observed, the mutual compensation of deviations
366 leads to very close integrated band intensities.

367 In the case of O₂-N₂, according to calculations, the integrated intensity, $S_{O_2-N_2}$, is mostly
368 independent of the temperature with a mean value around 70×10^{-6} cm⁻² amagat⁻² which falls within the
369 error bars of the FTS and CRDS values.

370 In the case of O₂-O₂, the calculated integrated $B_{O_2-O_2}$ coefficient is predicted to increase
371 significantly with the temperature (about 15% over ~60 K). This is about twice the increase rate measured
372 by CRDS while Maté et al. did not evidence any significant variation between 253 and 296 K.

373

	Temperature K	$S_{O_2-O_2}$ $10^{-6} \text{ cm}^{-2} \text{ amagat}^{-2}$	$S_{O_2-N_2}$ $10^{-6} \text{ cm}^{-2} \text{ amagat}^{-2}$	S_{O_2-air} $10^{-6} \text{ cm}^{-2} \text{ amagat}^{-2}$
This work	271.1	349.2(60)	73.3(25)	131.2(33)
Mondelain et al. (2019)	297.0	358.8(21) ^a	71.1(37)	131.4(29) ^a
This work	331.6	375.0(60)	71.6(25)	134.5(33)
Maté et al. (1999)	253.0	349.9(9)	73.7(20)	131.7(15)
	273.3	347.3(10)	67.8(25)	126.5(19)
	296.2	349.9(16)	67.9(36)	127.1(27)
Karman et al. (2018)	271/275/275 ^b	321.1 ^c	70.6	121.3
	296/298/298 ^b	341.6 ^c	70.9	124.9
	332/323/323 ^b	373.7 ^c	71.2	129.1

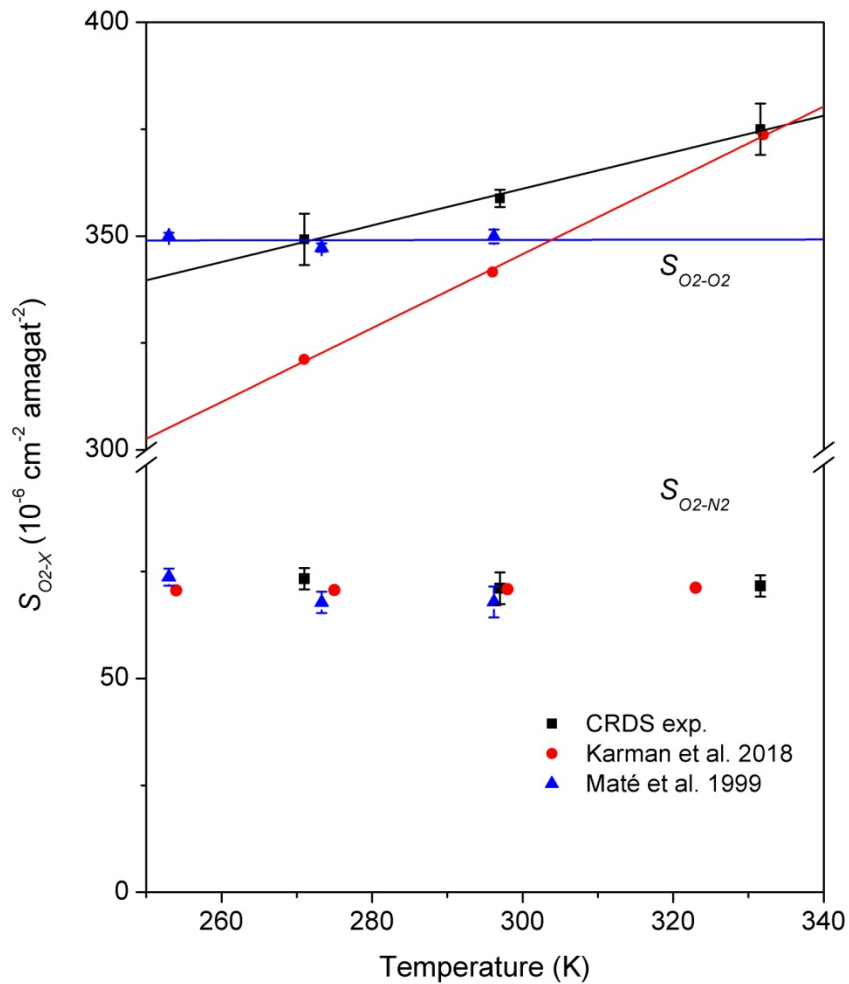
374 **Table 2.** Integrated binary coefficients derived from this work and from the literature. The numbers in
 375 parenthesis correspond to the 1σ uncertainties in unit of the last digit. The associated uncertainties were
 376 obtained by integrating the binary coefficients plus and minus their uncertainties.

377 ^a The given values of $S_{O_2-O_2}$ and S_{O_2-air} are smaller by 0.9 and 0.5 % compared than the value reported in Table
 378 1 of Mondelain et al. (2019), respectively, because, for comparison to the present work, the integration was limited
 379 to the 7546-8354 cm^{-1} interval, narrower than the 7515-8466 cm^{-1} considered in Mondelain et al. (2019),

380 ^b The temperatures correspond respectively to $S_{O_2-O_2}$, $S_{O_2-N_2}$ and S_{O_2-air} .

381 ^c Obtained using the *Supplementary Material* of Karman et al. (2018) and extended values given by T. Karman
 382 over the 7483-8482 cm^{-1} spectral range.

383



384

385 **Figure 8.** Evolution of the experimental and theoretical integrated intensities of the $S_{O_2-N_2}$ and $S_{O_2-O_2}$
 386 versus temperature.

387

388 It is important to mention that over the 270-332 K temperature range, the theoretical binary
 389 coefficients of Karman et al. (2018) evolves quasi-linearly with the temperature similarly to what we
 390 observe experimentally. When considering a larger temperature interval (e. g. between 200 K and 350 K),
 391 the calculations predict a quadratic dependence with temperature over some spectral ranges. We estimate
 392 that our experimental $B_{O_2-Air}(v_i)$ binary coefficients should be safely linearly extrapolated over the 250
 393 K-350 K temperature range.

394 **5. Conclusion and perspectives**

395 Spectra of pure O₂ and N₂-O₂ mixture were recorded at 271 K and 332 K over the 7550 – 8360 cm⁻¹
 396 spectral range thanks to a highly sensitive and stable cavity ring down spectrometer based on a newly
 397 developed temperature regulated high finesse optical cavity. The performances of the developed CRDS
 398 set-up, in particular its long term stability, allowed to accurately determine the small variation (a few %)
 399 of the CIAs with temperature. The $B_{O_2-O_2}$, $B_{O_2-N_2}$ and B_{O_2-air} binary absorption coefficients of the CIA
 400 retrieved from these spectra and the ones obtained at room temperature from our previous work
 401 (Mondelain et al., 2019) will allow to account for the variation of the CIA in the temperature range of the
 402 Earth's atmosphere.

403 Comparison to the calculations of Karman et al. (2018) shows a similar temperature dependence for
 404 $B_{O_2-N_2}$ while for $B_{O_2-O_2}$ significant differences are noted near the band center. The reported results
 405 provide constraints on the scaling factor of the line shapes for the spin-orbit and exchange mechanisms
 406 and could help to better estimate the exchange-induced dipole which has quite large uncertainty.

407 Our B_{O_2-air} coefficients are found in good agreement with results of Maté et al. (1999) obtained by
 408 FTS in different pressure conditions (up to 10 atm, while our CRDS spectra were recorded at pressures
 409 ranging between 300 and 700 Torr). Integrated binary coefficients over the entire band show almost no
 410 variation with temperature for O₂-N₂ CIA and an increase with temperature for pure O₂ CIA in qualitative
 411 agreement with the same quantities derived from calculations of Karman et al. (2018).

412 As *MicroCarb* instrument will use the B4 band between 7800-7912 cm⁻¹ to retrieve the surface
 413 pressure and then normalize the computed CO₂ column concentration, the impact of our new O₂ CIA data
 414 set on these quantities will be investigated using high signal-to-noise ratio and high resolution TCCON
 415 spectra with well-known pressure, temperature, humidity conditions and instrument characteristics. For
 416 that, spectra will be calculated with the Spectroscopic Parameters And Radiative Transfer Evaluation
 417 (SPARTE) chain (Armante et al., 2016), a calibration/validation chain, used to compare ground-based and
 418 space-borne observations. The direct radiative transfer calculations will be done by the 4A/OP code
 419 selected for the calibration/validation activities of *MicroCarb*.

420 It could also be useful to update the study of Zender (1999) on the solar absorption of oxygen
 421 collision complexes based on the new data set provided in this work and in Mondelain et al. (2019), for
 422 the CIA of the 1.27 μm band, and in the updated version of HITRAN (Karman et al., 2019). This will
 423 allow refining the radiative forcing due to oxygen collision pairs.

424 In a recent study, Baranov et al., (2012) and Hartmann et al. (2018) shown that the CIA of N₂ is
 425 importantly enhanced by water vapor. In this context, the magnitude of the O₂ CIA induced by
 426 atmospheric water vapor in wet atmospheres should also be investigated.

427

428 **Acknowledgements**

429 This work was supported by CNES in the frame of the *MicroCarb* project. Authors also want to
430 thank T. Karman for providing them unpublished calculations extending the CIA spectral range. DM
431 wants to thank S. Béguier for writing the program to calculate the temperature coefficients.

432

433 **Data Availability Statement**

434 The base line corrected CRDS spectra used in this work are available under:
435 <https://zenodo.org/badge/DOI/10.5281/zenodo.4562331.svg>

436 **References**

- 437 Armante R., Scott N., Crevoisier C., Capelle V., Crepeau L., Jacquinet N., & Chédin A. (2016). Evaluation of
438 spectroscopic databases through radiative transfer simulations compared to observations. Application to the
439 validation of GEISA 2015 with IASI and TCCON. *J Mol Spectrosc*, 327, 180-192. doi:10.1016/j.jms.2016.04.004
- 440 Badger, R. M., Wright, A. C., & Whitlock, R. F. (1965). Absolute intensities of the discrete and continuous
441 absorption bands of oxygen gas at 1.26 and 1.065 μm and the radiative lifetime of the 11g state of oxygen. *Journal*
442 *of Chemical Physics*, 43, 4345–4350.
- 443 Baranov, Y. I., Buryak, I. A., Lokshtanov, S. E., Lukyanchenko, V. A. & Vigasin, A. A. (2012). H₂O–N₂ collision-
444 induced absorption band intensity in the region of the N₂ fundamental: *ab initio* investigation of its temperature
445 dependence and comparison with laboratory data. *Phil. Trans. R. Soc. A*, 370, 2691–2709.
446 doi:10.1098/rsta.2011.0189
- 447 Berden, G., Peeters, R., & Meijer, G. (2000). Cavity Ring-Down Spectroscopy: Experimental schemes and
448 applications. *International Review in Physical Chemistry*, 19, 565–607. doi:10.1080/014423500750040627.
- 449 Bertaux, J.-L., Hauchecorne, A., Lefèvre, F., Jouget, D., Blanot, L., Bréon, F.-M., et al. (2018) Use of the 1.27 μm
450 O₂ absorption band for CO₂ and methane estimates in nadir viewing from space: Potential and application to
451 Microcarb. *Geophysical Research Abstracts*, 20, EGU2018-14935, EGU General Assembly 2018.
- 452 Blickensderfer, R. P., & Ewing, G. E. (1969). Collision-induced absorption Spectrum of Gaseous Oxygen at Low
453 Temperatures and Pressures. I. The $^1\Delta_g$ – $^3\Sigma_g$ System. *Journal of Chemical Physics*, 51, 873-883.
- 454 Campargue, A., Kassi, S., Mondelain, D., Vasilchenko, S., & Romanini, D. (2016). Accurate laboratory
455 determination of the near-infrared water vapor self-continuum: A test of the MT_CKD model. *Journal of*
456 *Geophysical Research: Atmospheres*, 121, D13180. doi:10.1002/2016JD025531.
- 457 Chagas, J. C. S., Newnham, D. A., Smith, K. M., & Shine, K. P. (2002). Impact of new measurements of oxygen
458 collision-induced absorption on estimates of short-wave atmospheric absorption. *Quarterly Journal of the Royal*
459 *Meteorological Society*, 128, 2377–2396. doi:10.1256/qj.01.159
- 460 Goody, R. M., & Yung, Y. L. (1989). *Atmospheric Radiation Theoretical Basis*, 2nd ed., New York, Oxford
461 University Press.
- 462 Cho, C. W., Allin, E. J., & Welsh, H. L. (1963). Effect of high pressures on the infrared and red atmospheric
463 absorption band systems of oxygen. *Canadian Journal of Physics*, 41, 1991–2002.
- 464 CNES (2018) : <https://microcarb.cnes.fr/en>
- 465 Dianov-Klokov, V. I. (1964). Absorption spectrum of oxygen at pressures from 2 to 35 atm in the region from
466 12600 to 3600 Å. *Optics and Spectroscopy (English Translation)*, 16, 224–227.
- 467 Gardner, J. P., Mather, J.C., Clampin, M., Doyon, R., Greenhouse, M. A., Hammel, H. B., et al. (2006). The James
468 Webb Space Telescope. *Space Science Reviews*, 123: 485–606. doi:10.1007/s11214-006-8315-7

- 469 Ghysels, M., · Liu, Q., Fleisher, A. J., & Hodges, J. T. (2017). A variable-temperature cavity ring-down
470 spectrometer with application to line shape analysis of CO₂ spectra in the 1600 nm region. *Applied Physics B*,
471 123,124. doi:10.1007/s00340-017-6686-y
- 472 Gordon, I. E., Kassı, S., Campargue, A., & Toon, G. C. (2010). First identification of the $a^1\Delta_g - X^3\Sigma_g^-(0-0)$
473 electric quadrupole transitions of oxygen in the solar and laboratory spectra. *Journal of Quantitative Spectroscopy &*
474 *Radiative Transfer*, 111, 1174-1183. doi:10.1016/j.jqsrt.2010.01.008
- 475 Gordon I. E., Rothman, L. S., Hill, C., Kochanov, R. V., Tan, Y., Bernath, P. F., et al. (2017). The HITRAN2016
476 Molecular Spectroscopic Database. *Journal of Quantitative Spectroscopy & Radiative Transfer*, 203, 3-69.
477 doi:10.1016/j.jqsrt.2017.06.038
- 478 Hartmann, J.-M., Boulet, C., Tran D.D., Tran, H. (2018) Effect of humidity on the absorption continua of CO₂ and
479 N₂ near 4 μm: Calculations, comparisons with measurements, and consequences for atmospheric spectra. *J. Chem.*
480 *Phys.*, 148, 054304. doi:10.1063/1.5019994)
- 481 Karman, T., van der Avoird, A., & Groenenboom, G. C. (2017). Line-shape theory of the $X^3\Sigma_g^- - a^1\Delta_g, b^1\Sigma_g^+$
482 transitions in O₂-O₂ collision-induced absorption. *Journal of Chemical Physics*, 147, 084307.
483 doi:10.1063/1.4990662
- 484 Karman, T., Koenis, M. A. J., Banerjee, A., Parker, D. H., Gordon, I. E., van der Avoird, A., et al. (2018). O₂-O₂
485 and O₂-N₂ collision-induced absorption mechanisms unraveled. *Nature Chemistry*, 10, 549-554,
486 doi:10.1038/s41557-018-0015
- 487 Karman, T., Gordon I. E., van der Avoird A., Baranov Y. I., Boulet C., Drouin B. J., et al. (2019). Update of the
488 HITRAN collision-induced absorption section. *Icarus*, 328, 160-175. doi:10.1016/j.icarus.2019.02.034
- 489 Kassı, S., Gao, B., Romanini, D. & Campargue, A. (2008). The near infrared (1.30-1.70 μm) absorption spectrum of
490 methane down to 77 K. *Phys. Chem. Chem. Phys.* 10, 4410-4419. doi:10.1039/B805947K
- 491 Kassı, S. & Campargue, A. (2012). A. Cavity ring down spectroscopy with 5×10^{-13} cm⁻¹ sensitivity. *Journal of*
492 *Chemical Physics*, 137, 234201, doi:10.1063/1.4769974.
- 493 Kassı, S., Campargue, A., Mondelain, D., & Tran, H. (2015). High pressure Cavity Ring Down Spectroscopy:
494 Application to the absorption continuum of CO₂ near 1.7 μm. *Journal of Quantitative Spectroscopy & Radiative*
495 *Transfer*. 167, 97-104. doi:10.1016/j.jqsrt.2015.08.014
- 496 Ketelaar, J. A. A. (1955). La transition triplet-singlet dans l'oxygene sous pression. *Nuovo Cimento*, II, suppl., ser X,
497 3, 763-765.
- 498 Konefał M., Kassı S., Mondelain D., & Campargue A. (2020). High sensitivity spectroscopy of the O₂ band at 1.27
499 μm: (I) pure O₂ line parameters above 7920 cm⁻¹. *Journal of Quantitative Spectroscopy & Radiative Transfer* 241,
500 106653. doi:10.1016/j.jqsrt.2019.106653

- 501 Lechevallier, L., Vasilchenko, S., Grilli, R., Mondelain, D., Romanini, D., & Campargue A. (2018). The water
502 vapour self-continuum absorption in the infrared atmospheric windows: new laser measurements near 3.3 and 2.0
503 μm . *Atmospheric Measurements Techniques*, 11, 2159–2171. doi:10.5194/amt-11-2159-2018.
- 504 Leshchishina, O., Kassi, S., Gordon, I. E., Rothman, R. L., Wang, L., & Campargue A. (2010). High sensitivity
505 CRDS of the $a^1\Delta_g - X^3\Sigma_g^-(0-0)$ band of oxygen near 1.27 μm : extended observations, quadrupole transitions,
506 hot bands and minor isotopologues, *Journal of Quantitative Spectroscopy & Radiative Transfer*, 111, 2236-2245.
507 doi:10.1016/j.jqsrt.2010.05.014.
- 508 Long, D.A., Havey, D.K., Okumura, M., Miller, C.E., & Hodges, J.T. (2010) O₂ A-band line parameters to support
509 atmospheric remote sensing. *Journal of Quantitative Spectroscopy & Radiative Transfer*, 111, 2021-2036.
510 doi:10.1016/j.jqsrt.2010.05.011
- 511 Maity, A., Maithani, S., & Pradhan M. (2021). Cavity Ring-Down Spectroscopy: Recent Technological
512 Advancements, Techniques, and Applications. *Anal. Chem.*, 93, 388–416. doi:10.1021/acs.analchem.0c04329.
- 513 Maté, B., Lugez, C., Fraser, G. T., & Lafferty W. J. (1999). Absolute intensities for the O₂ 1.27 μm continuum
514 absorption. *Journal of Geophysical Research: Atmospheres*, 104, D30585. doi:10.1029/1999JD900824.
- 515 McKellar, A. R. W., Rich, N. R., & Welsh H. L. (1972). Collision-induced vibrational and electronic spectra of
516 gaseous oxygen at low temperatures. *Canadian Journal of Physics*, 50, 1–9.
- 517 Mendonca, J., Strong, K., Wunch, D., Toon, G. C., Long, D. A., Hodges, J. T., et al. (2018) Improving the Retrieval
518 of XCO₂ from Total Carbon Column Network Solar Spectra. *Atmospheric Measurement Techniques*. 124, 414–423.
519 doi:10.5194/amt-2018-62
- 520 Misra, A., Meadows, V., Claire, M., & Crisp, D. (2014). Using Dimers to Measure Biosignatures and Atmospheric
521 Pressure for Terrestrial Exoplanets. *Astrobiology*, 14, 68-86. doi:10.1089/ast.2013.0990
- 522 Mlawer, E. J., Clough, S. A., Brown, P. D., Stephen, T. M., Landry, J. C., Goldman, A., & Murcray, F. (1998).
523 Observed atmospheric collision-induced absorption in near infrared oxygen bands. *Journal of Geophysical*
524 *Research: Atmospheres*, 103, D3859. doi:10.1029/97JD03141
- 525 Mondelain, D., Campargue, A., Čermák, P., Gamache, R.R., Kassi, S., Tashkun, S.A., & Tran, H. (2017). The CO₂
526 absorption continuum by high pressure CRDS in the 1.74 μm window. *Journal of Quantitative Spectroscopy &*
527 *Radiative Transfer* 203, 530–537. doi:10.1016/j.jqsrt.2017.02.019
- 528 Mondelain, D., Kassi, S., & Campargue, A. (2019). Accurate laboratory measurement of the O₂ collision-induced
529 absorption band near 1.27 μm . *J. Geophys. Res.: Atmospheres* 124,414–423. doi:10.1029/2018JD029317
- 530 Morville, J., Romanini, D., Kachanov, A. A., & Chenevier, M. (2004). Two schemes for trace detection using cavity
531 ring down spectroscopy. *Applied Physics B*, 78, 465–476. doi:10.1007/s00340-003-1363-8

- 532 Newnham, D. A., & Ballard, J. (1998). Visible absorption cross sections and integrated absorption intensities of
533 molecular oxygen (O_2 and O_4), *Journal of Geophysical Research: Atmospheres*, 103, D22, 28,801.
534 doi:10.1029/98JD02799
- 535 Ptashnik I. V. (2007). Evaluation of suitable spectral intervals for near-IR laboratory detection of water vapour
536 continuum absorption. *Journal of Quantitative Spectroscopy & Radiative Transfer*. 108, 146–160.
537 doi:10.1016/j.jqsrt.2007.03.011.
- 538 Richard, L., Vasilchenko, S., Mondelain, D., Ventrillard, I., Romanini, D., & Campargue, A. (2017). Water vapor
539 self-continuum absorption measurements in the 4.0 and 2.1 μm transparency windows, *Journal of Quantitative*
540 *Spectroscopy & Radiative Transfer*, 201, 171–179. doi:10.1016/j.jqsrt.2017.06.037
- 541 Romanini, D., Kachanov, A. A., Sadeghi, N., & Stoeckel, F. (1997). CW cavity ring down spectroscopy, *Chemical*
542 *Physics Letters*, 264, 316–322. doi:10.1016/S0009-2614(96)01351-61997.
- 543 Schwieterman, E. W., Olson, S. L., Reinhard, C. T., Ridgwell, A., Kane, S., Meadows, V. S., & Lyons, T. W. (2018).
544 Exoplanet Biosignatures: A Review of Remotely Detectable Signs of Life *Astrobiology*, 18,
545 doi:10.1089/ast.2017.1729
- 546 Smith, K. M., & Newnham, D. A. (1999). Near-infrared absorption spectroscopy of oxygen and nitrogen gas
547 mixtures, *Chemical Physics Letters*, 308, 1–6. doi:10.1016/S0009-2614(99)00584-9
- 548 Smith, K. M., & Newnham, D. A. (2000). Near-infrared absorption cross sections and integrated absorption
549 intensities of molecular oxygen (O_2 , O_2 - O_2 , and O_2 - N_2). *Journal of Geophysical Research*, 105, 7383-7396.
550 doi:10.1029/1999JD901171
- 551 Solomon, S., Portmann, R. W., Sanders, R. W., & Daniel, J. S. (1998) Absorption of solar radiation by water
552 vapour, oxygen, and related collision pairs in the earth's atmosphere, *Journal of Geophysical Research:*
553 *Atmospheres*, 103, D4, 3847–3858. doi:10.1029/97JD03285
- 554 Sun, K., Gordon, I. E., Sioris, C. E., Liu, X., Chance, K., & Wofsy, S. C. (2018). Re-evaluating the use of O_2 $a^1\Delta_g$
555 band in the spaceborne remote sensing of greenhouse gases, *Geophysical Research Letters*, 45, 5779–5787.
556 doi:10.1029/2018GL077823.
- 557 Tabisz, G. C., Allin, E. J., & Welsh, H. L. (1969). Interpretation of the visible and near-infrared absorption spectra
558 of compressed oxygen as collision-induced electronic transitions. *Canadian Journal of Physics*, 47, 2859-2871.
- 559 Thalman, R., Zarzana, K., Tolbert, M. A., & Volkamer, R. (2014). Rayleigh scattering cross-section measurements
560 of nitrogen, argon, oxygen and air, *Journal of Quantitative Spectroscopy & Radiative Transfer*, 147, 171–177.
561 doi:10.1016/j.jqsrt.2014.05.030.
- 562 Thalman, R., Zarzana, K., Tolbert, M. A., & Volkamer, R. (2017). Erratum to “Rayleigh scattering cross-section
563 measurements of nitrogen, argon, oxygen and air” *J. Quant. Spectrosc. Radiat. Transfer* 147 (2014) 171-177,
564 *Journal of Quantitative Spectroscopy & Radiative Transfer*, 189, 281-282. doi:10.1016/j.jqsrt.2016.12.014

- 565 Tran, D.D., Tran, H., Vasilchenko, S., Kassi, S., Campargue A., & Mondelain, D. (2020). High sensitivity
566 spectroscopy of the O₂ band at 1.27 μm: (II) air-broadened line profile parameters, *Journal of Quantitative*
567 *Spectroscopy & Radiative Transfer*, 240, 106673. doi:10.1016/j.jqsrt.2019.106673
- 568 Tran, D. D., Delahaye, T., Armante, R., Hartmann, J.-M., Mondelain, D., Campargue, A., Fleurbaey, H., Hodges, J.
569 T., Tran, H. (2021). Validation of spectroscopic data in the 1.27 μm spectral region by comparisons with ground-
570 based atmospheric measurements. *Journal of Quantitative Spectroscopy & Radiative Transfer*, 261, 107495.
571 doi:10.1016/j.jqsrt.2020.107495
- 572 Washenfelder, R. A., Toon, G. C., Blavier, J.-F., Yang, Z., Allen, N. T., Wennberg, P. O., et al. (2006), Carbon
573 dioxide column abundances at the Wisconsin Tall Tower site. *Journal of Geophysical Research: Atmospheres*, 111,
574 D22305. doi:10.1029/2006JD007154.
- 575 Wunch, D., Toon, G. C., Blavier, J.-F. L., Washenfelder, R. A., Notholt, J., Connor, B. J., et al. (2011) The Total
576 Carbon Column Observing Network. *The Philosophical Transactions of the Royal Society A*, 369, 2087–2112.
577 doi:10.1098/rsta.2010.0240
- 578 Zender, C. S. (1999). Global climatology of abundance and solar absorption of oxygen collision complexes. *Journal*
579 *of Geophysical Research: Atmospheres*, 104, D20, 24471–24484. doi:10.1029/1999JD900797
- 580